Nuclear Science and Techniques (2026) 37:20
https://doi.org/10.1007/s41365-025-01856-4

Impedance of RF shield on ceramic chamber in the rapid cycling synchrotron of China Spallation Neutron Source

Liang-Sheng Huang[1,2,3] · Bin Wu[1,2] · Ming-Yang Huang[1,2,3] · Ren-Hong Liu[1,2] · Biao Tan[1,2] · Peng-Cheng Wang[1,2] · Yong-Chuan Xiao[1,2] · Li-Rui Zeng[1,2,3] · Xiao Li[1,2,3]

Received: 25 November 2024 / Revised: 15 February 2025 / Accepted: 2 March 2025 / Published online: 10 December 2025

Abstract

In a rapid cycling synchrotron (RCS), the magnetic field is synchronized with the beam energy, creating a highly dynamic magnetic environment. A ceramic chamber with a shielding layer (RF shield), composed of a series of copper strips connected to a capacitor at either end, is typically employed as a vacuum chamber to mitigate eddy current effects and beam coupling impedance. Consequently, the ceramic chamber exhibits a thin-walled multilayered complex structure. Previous theoretical studies have suggested that the impedance of such a structure has a negligible impact on the beam. However, recent impedance measurements of the ceramic chamber in the China Spallation Neutron Source (CSNS) RCS revealed a resonance in the low-frequency range, which was confirmed by further theoretical analysis as a source of beam instability in the RCS. Currently, the magnitude of this impedance cannot be accurately assessed using theoretical calculations. In this study, we used the CST Microwave Studio to confirm the impedance of the ceramic chamber. Further simulations covering six different types of ceramic chambers were conducted to develop an impedance model in the RCS. Additionally, this study investigates the resonant characteristics of the ceramic chamber impedance, finding that the resonant frequency is closely related to the capacitance of the capacitors. This finding provides clear directions for further impedance optimization and is crucial for achieving a beam power of 500 kW for the CSNS Phase-II project (CSNS-II). However, careful attention must be paid to the voltage across the capacitors.

Keywords Beam coupling impedance · Ceramic chamber · RF shield · Resonance · High dynamic magnetic environment

1 Introduction

The China Spallation Neutron Source (CSNS) is a high-intensity proton accelerator-based facility [1, 2] designed to provide multidisciplinary platforms for scientific research and applications [3–6]. The accelerator complex consists of two primary components: a negative hydrogen (H^-) linac [7–10] and a rapid cycling synchrotron (RCS) [11]. The H^- beam from the linac is injected into the RCS through a multiturn charge-exchange process [12]. Within the RCS, two proton bunches, with a total of $N_p = 1.56 \times 10^{13}$ per pulse, are accelerated from 80 MeV to 1.6 GeV at a repetition rate of 25 Hz. Currently, the RCS provides a beam power of 100 kW on the target. In the Phase-II of the CSNS (CSNS-II), the beam power on the target will be upgraded from 100 kW to 500 kW by increasing the beam intensity. The RCS is dominated by space charge effects. To address these issues, superconducting cavities will be utilized to

This work was supported by the Guangdong Basic and Applied Basic Research Foundation, China (No. 2021B1515140007).

✉ Liang-Sheng Huang
huangls@ihep.ac.cn

✉ Xiao Li
lixiao@ihep.ac.cn

[1] Spallation Neutron Source Science Center, Dongguan 523803, China

[2] Institute of High Energy Physics, CAS, Beijing 100049, China

[3] University of Chinese Academy of Sciences, Beijing 100049, China

Table 1 Main parameters of RCS

Parameters	Values
Circumference (m)	227.92
Injection energy of CSNS/CSNS-II (GeV)	0.08/0.3
Extraction energy (GeV)	1.6
Repetition rate (Hz)	25
Ramping pattern	Sinusoidal
dB/dt (T/s)	63
Number of ceramic chambers	76
Bunch number	2
Bunch intensity of CSNS/CSNS-II (1×10^{12})	7.8/39
Nominal tune (H,V)	(4.86,4.78)
Natural chromaticity (H,V)	(−4.2,−9.1)

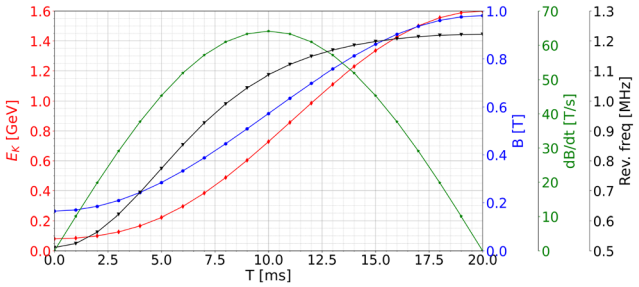

Fig. 1 (Color online) Ramping energy, magnetic curve and change rate of magnetic field in CSNS/RCS

boost the linac beam energy from 80 MeV to 300 MeV, mitigating the space charge effects in the RCS. Following these upgrades, the accumulated number of protons in the RCS is expected to reach $N_p = 7.8 \times 10^{13}$ per pulse.

Table 1 presents the main parameters of the RCS, which employs a triplet fourfold symmetric lattice structure with a circumference of 227.92 m. It consists of 24 dipole magnets and 48 quadrupole magnets, energized by a 25 Hz DC-biased sinusoidal current pattern [13, 14]. The RCS has a nominal tune of (4.86, 4.78) and natural chromaticity of (−4.2, −9.1). The DC sextupole field was designed to improve chromaticity control and minimize beam loss during injection. The magnetic field is synchronized with the beam energy, resulting in a highly dynamic magnetic environment. Figure 1 depicts the ramping energy, magnetic field curve, and its rate of change. The acceleration ramp was characterized by a standard sine wave, with a magnetic field change rate exceeding 60 T/s.

Owing to the heating of eddy current effects [15], traditional metal chambers are inadequate in such a dynamic magnetic environment of the RCS; hence, ceramic chambers are employed. The main part of the chamber was made of ceramic. To mitigate the leakage field induced by the beam due to the non-conductive nature of the ceramic chambers, an RF shield was used to reduce the eddy current effects and beam coupling impedance. These ceramic chambers are used in magnets with a high dynamic magnetic field. A ceramic chamber [16] at the CSNS was designed based on an existing chamber [17, 18]. The inner surface of the ceramic chamber was coated with a TiN film to reduce the secondary electron emission. Surrounding the ceramic, an RF shield is composed of a series of copper strips and capacitors, creating a high-pass filter that mitigates eddy current effects and reduces beam coupling impedance. The ceramic chamber occupies approximately 130 m of the RCS, whereas stainless-steel chambers occupy the remaining space.

Beam instability associated with ceramic chambers has been observed in RCS facilities worldwide. The head–tail effects [19] were identified in the RCS of ISIS [17] many years ago, and the ceramic chamber has recently been implicated as a potential contributor to impedance [20]. In the RCS of the Japan Proton Accelerator Research Complex (J-PARC) [18], an instability [21] was detected during beam commissioning, appearing before 2 ms when the horizontal and vertical tunes were set to $\nu_x = \nu_y = 5.86$. This beam behavior is analogous to that observed in the RCS of CSNS.

In 2019, the RCS of CSNS experienced an unforeseen instability in the transverse plane as beam power was gradually increased from 20 kW to 50 kW, with the instability worsening at higher power levels [22]. Measurements identified this issue as a transverse coupled bunch instability (TCBI). To address this, tune tracking pattern adjustments and chromaticity optimization using DC-powered sextupole magnets were applied, successfully achieving the designed beam power of CSNS [22, 23]. In 2021, DC sextupole magnets were replaced with AC versions and their associated power supplies [24], providing dynamic chromaticity control over the acceleration cycle. Furthermore, a pulsed octupole magnet was proposed and developed in summer 2023 to mitigate instability under increased beam power. With the aid of AC sextupole and pulsed octupole magnets, the RCS beam power was increased to 160 kW. Despite these improvements, the beam power has reached the limits of current mitigation strategies, presenting a considerable challenge to the 500 kW objective of CSNS-II. Additionally, the inability to accurately identify the sources of impedance remains a critical issue. If the components contributing to impedance are precisely identified, reducing their impedance could provide a fundamental strategy for increasing beam power, surpassing the effectiveness of existing suppression methods.

The driving forces behind beam instabilities in accelerators depend on the interaction between charged particles and their environment, which is typically described by the beam coupling impedance [25–27]. The RCS of CSNS incorporates components that are widely used and have been effective in other accelerator systems. Despite this, we conducted

an extensive impedance analysis for each component of the RCS [28]. Notably, instabilities originating from the stainless-steel chamber [29] and extraction kicker [30] were anticipated to be negligible. Furthermore, the real part of impedance from ceramic chambers [31, 32] was expected to be minimal. It should be noted that the ceramic chamber was modeled as an infinitely long, multilayered structure with perfect RF shielding, which significantly differed from the actual RF shielding setup.

Recent bench measurements have confirmed that the RF shield on the ceramic chamber is a source of impedance [33]. This represents a novel source of impedance with relatively limited international research to date. The earliest work on infinitely long ceramic chambers was conducted by Zotter [34] in 1970. Since then, the model has primarily evolved, particularly in the field matching method for both relativistic and non-relativistic particles [35–38]. Danilov developed an impedance model to estimate the impedance of a finitely long chamber [39]. In these models, the electromagnetic fields are assumed to be fully shielded by metal strips, resulting in a very low calculated impedance with no predicted resonances. Given the limitations of theoretical calculations, this study employed CST Microwave Studio [40] to simulate the impedance of the ceramic chamber. The simulation validated the existence of resonant impedance and allowed for the determination of the impedance characteristics for all ceramic chambers in the RCS.

The remainder of this paper is organized as follows: Section 2 provides a brief overview of RCS instability characteristics. Section 3 reports preliminary impedance measurements of a ceramic chamber. Section 4 discusses the simulation techniques used to evaluate ceramic chamber impedance and calculates the total impedance for the RCS. The simulations indicated an unexpectedly high impedance in the RCS, which presents a substantial challenge for the CSNS-II project. As a result, Sect. 5 explores chamber parameters to identify effective impedance reduction methods. The findings suggest that optimizing capacitor capacitance is an effective technique, with capacitor voltage being a key factor. Consequently, Sect. 6 provides a detailed theoretical analysis of capacitor voltage, serving as a reference for subsequent impedance reduction practices. The study is summarized and discussed in Sect. 7.

2 Characteristic of the RCS instability in CSNS

The instability in the RCS was observed at a beam power of approximately 50 kW. Beam measurements confirmed that it was a TCBI. Under normal tune and natural chromaticity, the beam position in the horizontal plane began to oscillate at around 8 ms. This instability was found to be dependent on the beam population, regardless of whether particles were filled into single or double buckets. The coupled bunch mode was identified as mode one, which means that the betatron oscillation of the two bunches was out of phase. The instability exhibited sensitivity to chromaticity, prompting the introduction of sextupole magnets to mitigate this problem. The horizontal tune also had a significant impact on this instability. Figure 2 illustrates the measured turn-by-turn (TbT) beam positions and transmission efficiency in the RCS at different tunes with a beam power of 100 kW. The instability is observed when the tune is below 5.0, and its occurrence time shifts later as the tune increases. Furthermore, with tested tune during the beam commissioning, the instability in vertical plane can also be observed as beam power increases. If there are M identical equally spaced bunches, the growth rate of the coupled bunch instability $1/\tau_m$ can be theoretically expressed as [41]

$$\frac{1}{\tau_m} = -\frac{eMI_b\omega_0}{4\pi\beta E_0}\frac{\sum_q Re[\beta_\perp Z_T(\omega_q)]h_m}{B\sum_q h_m}F_m, \tag{1}$$

where e is the electronic charge, I_b is the bunch current and ω_0 is the revolution angular frequency. E_0 is the beam

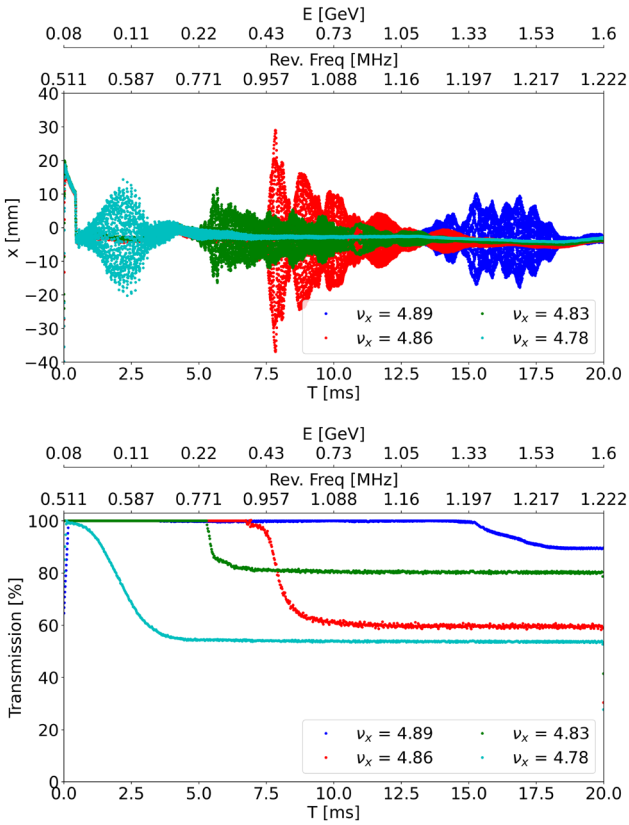

Fig. 2 (Color online) The TbT beam position (top) and RCS transmission efficiency (bottom) at different horizontal tunes with natural chromaticity at a beam power of 100 kW. The vertical tune is kept at 4.75

energy with a relativistic velocity factor β. $\beta_\perp$ is average betatron function. B is the bunching factor, defined as the ratio of bunch length to bunch spacing. With coupled mode μ, $Z_T(\omega_q)$ is the impedance magnitude at frequency $\omega_q = ((qM + \mu) + \nu_x + m\nu_s)\omega_0$ with a synchronous tune ν_s. For the head–tail mode m, h_m is the power spectrum with the form factor F_m, as specified in Ref. [41]. Within the RCS, $q = -3$, $M = 2$, $\mu = 1$, and $m = 1$, Table 2 roughly summarizes the instability occurrence time, energy, β, revolution frequency f_0, tune and $\omega_q/2\pi \approx 0.13$ MHz.

Our comprehensive studies provide valuable insights and practical guidance for mitigating instability, particularly through the optimization of the tune and chromaticity [23, 33]. To achieve better control over the tune spread and further suppress the instability, the DC sextupole field was upgraded to an AC sextupole field [24], aiming to provide dynamics for controlling the chromaticity and enhancing the beam transmission efficiency over an acceleration cycle.

3 Bench measurement of a ceramic chamber

To mitigate eddy current effects and ohmic losses, ceramic chambers are employed in AC magnets, including the dipole, quadrupole and injection painting magnets in the RCS of CSNS. As detailed in reference [16] and shown in Fig. 3, these chambers feature a three-layer tube design. The inner surface was coated with a 100 nm layer of titanium nitride (TiN) to reduce the secondary electron emission. Given the non-conductive nature of ceramics, an RF shield composed of 0.4 mm thick Cu plates, waterjet-cut into 5 mm wide strips with 5 mm spacing, was utilized to decrease the impedance of the image current. Each Cu strip was segmented to prevent current loops, effectively suppressing the eddy current effects. Furthermore, connecting the strip segments with capacitors (with a capacitance of 330 nF) creates an RF shield with a high-frequency pass filter, which reduces both eddy current effects and beam coupling impedance. Table 3 summarizes the shapes, lengths, and thicknesses of the chambers. An elliptical chamber is used for the dipole magnet, whereas circular cross-sectional chambers are employed for the others. The RCS comprises six types of ceramic chambers, with a total length of approximately 130 m, distributed across 76 units.

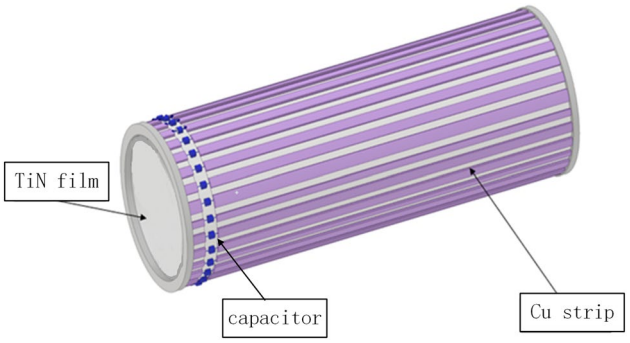

Fig. 3 (Color online) Illustration of the ceramic chamber

To identify the impedance, a ceramic chamber located in the injection area (INB1) was used to measure the impedance. The conventional wire method was employed for the coupling impedance measurements. For transverse impedance measurements, the standard technique involves the twin-wire method, where two parallel wires carrying out-of-phase signals are inserted through the device under test (DUT) to generate a dipole current moment, and the forward scatter coefficient, S_{21}, is measured covering the frequency range < 100 MHz. We did not observe unexpected impedance in such frequency range. However, due to significant measurement errors associated with the twin-wire method at low frequencies, the loop method is more suitable for this measurement, as illustrated at the top of Fig. 4. The equipment for the loop measurements included a vector network analyzer (VNA), a hybrid and the DUT. An out-of-phase signal is generated by the hybrid. The loop probe comprised two parallel wires with shorted ends. The spacing Δ of the Cu wires is 40 mm, with a wire diameter of 0.5 mm. The

Table 2 Overview of key parameters for RCS instability, roughly closed to the biggest oscillation amplitude of beam position, where $f_r = \omega_q/2\pi$ at $q = -3$, $M = 2$, $\mu = 1$ and $m = 1$

Parameter	ν_x=4.78	ν_x=4.83	ν_x=4.86	ν_x=4.89
Occurrence time (ms)	~ 2	5	7.0	~ 14
E_0 (GeV)	0.11	0.22	0.42	1.3
β	0.441	0.585	0.722	0.905
f_0 (MHz)	0.58	0.77	0.95	1.19
ν_s	0.01	0.0085	0.005	0.002
f_r (MHz)	0.127	0.131	0.132	0.13

Table 3 Parameters of the RCS ceramic chamber

Name	Shape	Length (m)	Size (mm)	Thickness (mm)	Number
MB[a]	elliptic	2.775	218×135	15×8.5	24
QA	circular	0.78	91.5	7.5	16
QB	circular	1.535	124.5	7.5	16
QC	circular	1.54	99.5	7.5	8
QD	circular	1.205	115	7.5	8
INB[b]	circular	1.1	80	7.5	4

[a]The size and thickness mean horizontal × vertical size for MB with an elliptic cross section

[b]There are two similar types of injection chambers, and simplifies as one here

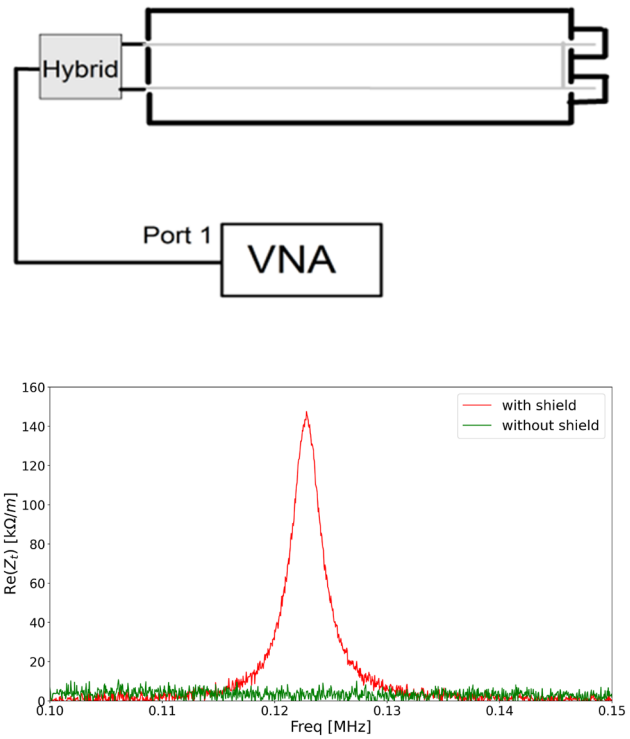

Fig. 4 (Color online) Schematic setup of the transverse impedance measurement with one loop method (top) and measured real part of INB1 transverse impedance (bottom)

reflection coefficient, S_{11}, is measured and the input impedance for DUT, $Z_{\text{in}}^{\text{DUT}}$, is given [42]

$$Z_{\text{in}}^{\text{DUT}} = \frac{2Z_0 S_{11}}{1 - S_{11}}, \tag{2}$$

with a characteristic impedance Z_0. The transverse impedance can be expressed as [43]

$$Z_{\text{T}} = \frac{c}{\omega} \frac{Z_{\text{in}}^{\text{DUT}} - Z_{\text{in}}^{\text{REF}}}{\Delta^2}, \tag{3}$$

with the measured frequency ω and the speed of light c. The measured input impedance, $Z_{\text{in}}^{\text{REF}}$, corresponds to a smooth, homogeneous beam chamber of equal length (REF), using the ceramic chamber without the RF shield as the REF in the measurement.

The impedance < 10 MHz was measured, and a sharp resonance peak was detected. The real part of the impedance is presented in the bottom of Fig. 4. The center frequency is 0.123 MHz, aligning perfectly with the beam measurement results, ~ 0.13 MHz. To investigate the source further, the RF shield was removed during the measurement, leading to the disappearance of the resonance. Notably, the INB1 chamber measured was not coated by the TiN film. Impedance measurements were repeated after TiN coating, and the impedance persisted. Consequently, it was determined that the resonance originated from the RF shield.

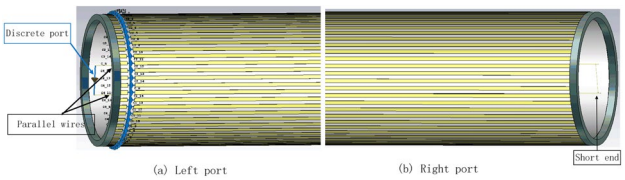

Fig. 5 (Color online) Simulated model of the ceramic chamber

4 Numerical simulation

To verify the impedance of the ceramic chamber, numerical simulations were conducted using the CST simulation suite. Actually, the wake field of ceramic chamber was simulated using Particle STUDIO many years ago, but no resonance was detected. In contrast, a simulation with Microwave Studio recently revealed the resonance. This discrepancy may be from meshgrids: Particle STUDIO employs only hexahedral meshgrid in the time domain, while Microwave Studio utilizes tetrahedral meshgrid in the frequency domain (The hexahedral meshgrid is unsuitable for capacitors in the frequency domain.). To further investigate this phenomenon, a time-domain model with hexahedral meshgrids was constructed in Microwave Studio and recomputed; however, resonance remained undetected. This hypothesis will be further investigated as the software is upgraded.

In the simulation, several reasonable simplifications were applied to develop a physical model that closely resembled the actual chamber. A simplified representation of the chamber is shown in Fig. 5. The primary components of the chamber included ceramic and two titanium ports at each end, consistent with a real chamber. The thin TiN film inside is not shown. The RF shield covering the ceramic consisted of Cu strips and capacitors, consistent with the actual design. We assumed that the capacitor had a loss of 0.09 Ω. The Kapton film, used in the real chamber for its high radiation resistance, was ignored owing to its non-conductive nature. The chamber length is 1.07 m. A loop probe, similar to that in the measurement, was incorporated in the simulation using two parallel wires with shorted ends, matching the 0.5 mm diameter of the measurement wires. A discrete port was provided to calculate the reflection-scattering coefficient at the open port. The size of the meshgrid was automatically adjusted based on regional dimensions, thereby improving calculation accuracy and optimizing memory and time usage. Approximately one million meshgrids were used to ensure precise results. A REF simulation was performed on a stainless-steel chamber of equal length.

The input reflection coefficients for both the DUT and REF were simulated, and the corresponding input impedances are provided in Eq. (2). The simulated impedance of the ceramic chamber is expressed as follows (Eq. (3)), as illustrated in Fig. 6. To enhance clarity, the measured results from Fig. 4 are also displayed. The resonant frequency identified closely corresponded to the measured results, thereby confirming the impedance in the simulation.

After accurately confirming the INB1 impedance, we simulated the impedances of all the chamber types in the RCS and developed a comprehensive impedance model that included all the ceramic chambers, as illustrated in Fig. 7. Each ceramic chamber exhibited resonance in the low-frequency range, with resonant frequencies varying among the different chambers. Table 4 provides a detailed summary of the resonant parameters of all the chambers in the RCS. The resonant frequencies range from 70 kHz to 150 kHz, with Q-values below 150. The MB chamber in the dipole magnet exhibited the highest impedance, reaching 6 MΩ/m.

In our simulations, we employed a monitor to evaluate the electromagnetic fields at the resonant frequency. The findings indicate that the induced electromagnetic field predominantly propagates along the Cu strips, with some leakage beyond the vacuum chamber. Such leakage may cause disturbances owing to external magnet yokes, thereby influencing the resonance. The ceramic chambers in the RCS are predominantly surrounded by dipole and quadrupole magnets. To explore this phenomenon, simplified models of the magnet yokes were developed and modeled as perfect electric conductors (PEC) with a thickness of 20 mm. The resonant frequencies of the chamber with and without the yokes are compared in Table 4. The results demonstrate that the presence of the yokes induces a shift in resonance frequency, which varies among different chamber configurations. For chambers with circular cross sections, the yoke-induced frequency shift is negligible.

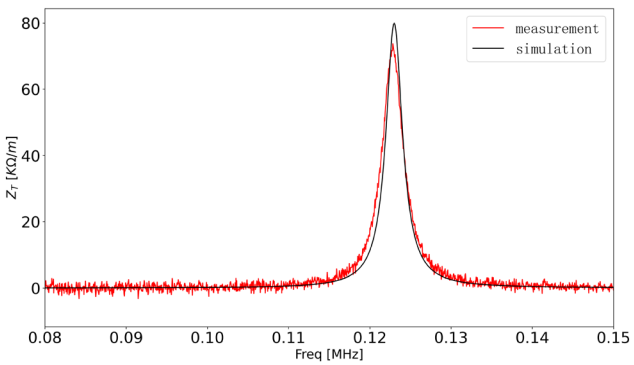

Fig. 6 (Color online) Simulated transverse impedance of the INB1 and compared with that of measurement

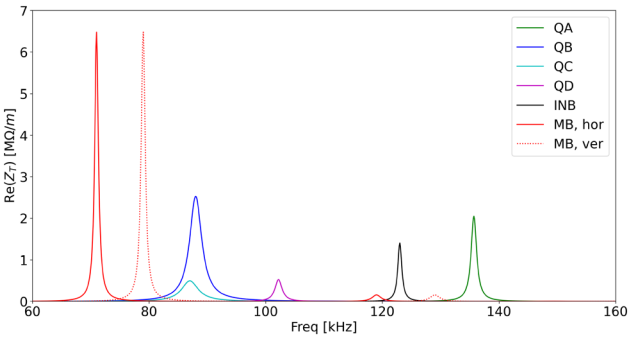

Fig. 7 (Color online) Impedance of all ceramic chambers in the RCS. Because of the circular cross section for MB chamber, the horizontal impedance differs from the vertical impedance

However, for the MB chamber with an elliptical cross section, where the yoke is 2.1 m long and closely aligned with the chamber in the vertical plane, the resonant frequency increases significantly, reaching approximately 35 kHz, indicating a substantial effect.

5 Investigation of impedance reduction techniques

The unusually high impedance, as illustrated in Fig. 7, explains the instability encountered during the RCS beam commissioning at low power levels. Achieving the design power target of 500 kW for CSNS-II requires a reduction in the ceramic chamber impedance in the RCS. Accordingly, we conducted a series of simulation studies to explore effective impedance reduction strategies. In this context, the feasibility and cost-effectiveness of these techniques are critical. Therefore, our objective was to identify the most dependable methods for impedance reduction, rather than focusing exclusively on the optimal solution.

Using INB1 as a reference, we performed detailed scans of various parameters, such as the strip number, width and thickness, along with the chamber radius and length

Table 4 Comparison of resonance frequency between ceramic chamber with and without yoke

Name	f_r without yoke (MHz)	f_r with yoke (MHz)
MB, Z_h	0.071	0.085
MB, Z_v	0.079	0.114
QA	0.136	0.141
QB	0.088	0.098
QC	0.087	0.1
QD	0.102	0.109
INB	0.123	0.127

and capacitor capacitance. The simulations demonstrated that the resonant frequency was mostly unaffected by the strip number, width and thickness, as well as the chamber radius. Rather, it is determined by the length of the ceramic chamber and the capacitance of the capacitors.

The impedance for various chamber lengths was examined, showing a decrease in the resonant frequency with increasing vacuum chamber length. However, because the chamber length is fixed in practical accelerators, this aspect will not be further explored in this study. Moreover, the resonant impedance for different capacitor capacitances was also simulated, and the results are displayed at the top of Fig. 8. It is evident that as the capacitance increases, both the resonant frequency and peak impedance decrease. The lower figure provides a summary of the resonant frequencies for various capacitances. With a given capacitance of the capacitor C, the resonant frequency is calculated theoretically by

$$f_{\mathrm{r}} = \frac{1}{2\pi\sqrt{L_0 C}}, \tag{4}$$

with a constant inductance $L_0 = 1.0146 \times 10^{-5}$ H. The calculated resonances showed excellent agreement with the simulation results, suggesting that the impedance issue can be simplified by addressing the inductance of the RF shield.

In summary, the simulations demonstrate that adjusting the capacitance of the capacitors can effectively reduce the impedance. Nonetheless, careful experimental validation is essential before applying this strategy to the RCS to ensure its reliability, particularly the voltage across the capacitors.

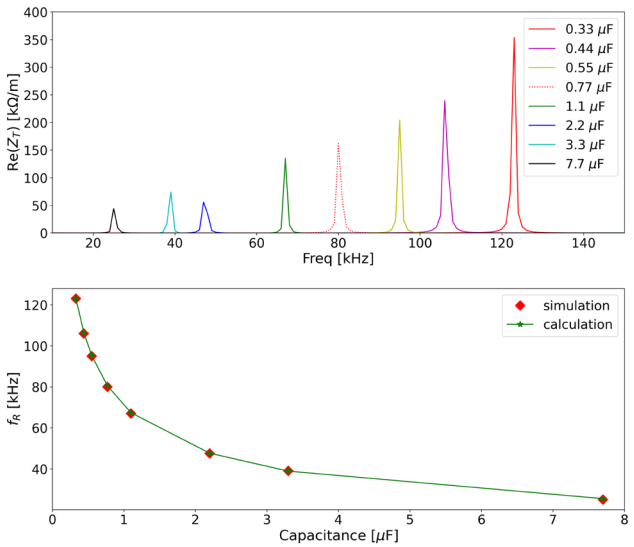

Fig. 8 (Color online) The top figure presents the simulated impedance across different capacitance values. The bottom figure compares the simulated resonant frequency on them with theoretical calculations by $f_{\mathrm{r}} = \frac{1}{2\pi\sqrt{L_0 C}}$, with a fitted inductance $L_0 = 1.0146 \times 10^{-5}$ H

6 Induced voltages on capacitors

During the ramping process in the RCS, voltages are induced on the capacitors. If these voltages exceed the rated threshold, capacitor failure may occur, leading to distortions in the magnetic field and subsequent beam instability. This instability has been empirically observed in the RCS of J-PARC as a result of these field distortions [44]. The voltage on capacitors was generated by both the beam and the dynamic magnetic field. In accelerators, circular vacuum chambers are the predominant structural configuration. Therefore, this study focuses on examining the voltage within circular cross sections.

6.1 Voltages on capacitors from dynamic magnetic field

The induced electromotive force, V, is proportional to the rate of change of magnetic flux linking the circuit, as dictated by Faraday's law of electromagnetic induction

$$V = -\frac{\mathrm{d}(B \cdot S)}{\mathrm{d}t}, \tag{5}$$

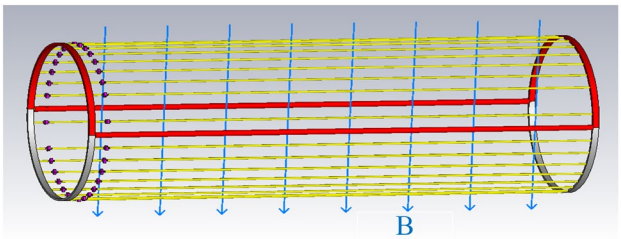

(a) Original coil: two stripes and the flanges on both sides of the chamber

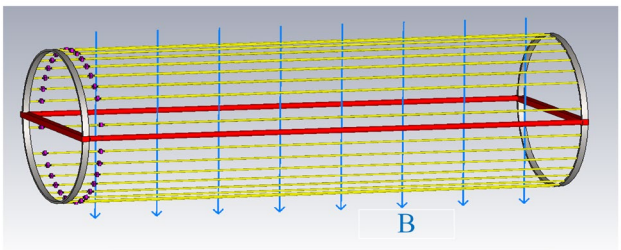

(b) Simplified coil: two stripes and simplified ends

Fig. 9 (Color online) The schematic picture of coil with the biggest area on the RF shield of ceramic chamber. **a** is the original coil and **b** is the simplified one

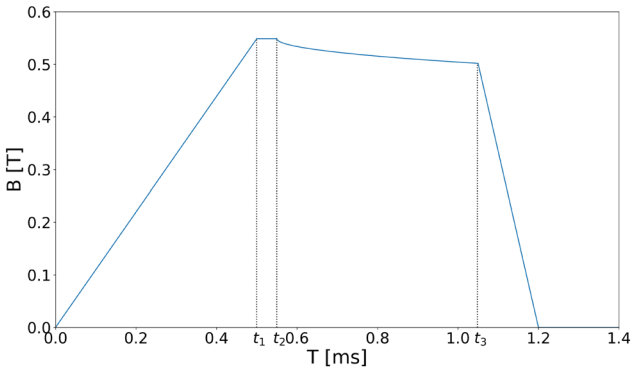

Fig. 10 (Color online) The typical magnetic field profile of the painting magnets in the RCS of CSNS

Table 5 The voltage on the capacitor of ceramic chamber

Chamber in magnet	dB/dt (T/s)	Volt (V)
Dipole magnet	60	27.5
Quadrupole magnet	61	15
Painting magnet	3660	314

with the time rate of change of magnetic field dB/dt and the cross-sectional area of a strip circuit S. The inner radius of the cylindrical RF shield is denoted by r. For simplicity, we focused on the central plane, which maximizes the cross-sectional area, as shown in Fig. 9a. We assume that the longitudinal magnetic field components can be neglected, which allows us to simplify Fig. 9a to the form shown in Fig. 9b. Furthermore, we consider only the case where the strip is cylindrical with a radius b, and the cross-sectional area S can be expressed as $S = 2(r + b)L$ with a magnet length L. Generally, because $r \gg b$ the area can be approximated as $S = 2rL$.

In the RCS of CSNS-II, a transverse painting technique was utilized during injection to ensure beam uniformity and reduce space charge effects. A new rectangular chamber (BCH) with a larger size of 245 mm × 167 mm and length of 0.44 m will be implemented. The injection system comprises horizontal and vertical painting magnets. The painting magnetic field exhibited the highest temporal rate of change. As illustrated in Fig. 10, the typical magnetic field profile for these magnets includes a rise time (from 0 to t_1), a flat-top time (from t_1 to t_2), a painting time (from t_2 to t_3) and a fall time (from t_3 to 1.2 ms). During the fall phase, the rate of change of the magnetic field reached a peak of dB/dt =3660 T/s, inducing a voltage of approximately 320 V, thereby justifying the use of capacitors. Additional evaluations were conducted to determine the voltage that the capacitors on all vacuum chambers must withstand, considering the dimensions of the RCS vacuum chamber and the change rate of magnetic field, as detailed in Table 5. It is clear that, apart from the injection region, the voltage endured by other capacitors is significantly lower.

6.2 Voltages on capacitors from beam

When the beam travels along the ceramic chamber, the beam current is easily given as

$$I = \hat{\lambda} e \beta c, \tag{6}$$

where e is the electric charge, and β is the relativistic velocity factor. For Gaussian beam with bunch length σ_z, the peak line charge density $\hat{\lambda}$ can be expressed [25] as

$$\hat{\lambda} = \frac{N_b}{\sqrt{2\pi}\sigma_z}, \tag{7}$$

with the particle number in the bunch N_b. The Gauss's law gives the electric field at strips with distance r as

$$E = \frac{\hat{\lambda} e}{2\pi\varepsilon_0 r}, \tag{8}$$

with a dielectric constant ε_0. Because the beam line charge induces image charges on the strips, the electric field outside the vacuum chamber remains zero. Therefore, the line density of image charges is

$$\sigma_s = \varepsilon_0 E = \frac{\hat{\lambda} e}{2\pi r}. \tag{9}$$

For a monopole beam located at the center of the chamber, the total induced image charge on the chamber is accurately equal to the charge of the source beam as $2\pi r \cdot \sigma_s = \hat{\lambda} e$, thus ensuring self-consistency. In practice, the shield of the chamber is composed of several strips. It was assumed that the leakage of the magnetic field beyond the chamber was negligible. Therefore, Eq. (9) can be simplified to

$$\sigma_s = \frac{\hat{\lambda} e}{N_s}, \tag{10}$$

with a strip number N_s. The current on the strip is $I_s = I/N_s$. For the dipole beam with a shift x in the horizontal plane in Fig. 11, we typically have $x \ll r$ and the voltage varies across different strips. A cylindrical coordinate system (r, θ) was adopted to describe the chamber with a circular cross section, with θ as the azimuthal coordinate. The strip positions are given by $(r\cos\theta, r\sin\theta)$. The distance from the strips to the beam is described as

$$d = \sqrt{x^2 - 2rx\cos\theta + r^2}, \tag{11}$$

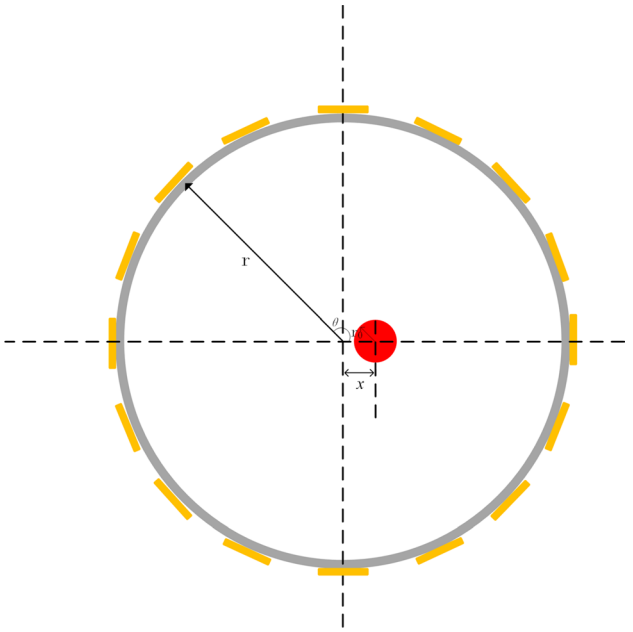

Fig. 11 (Color online) The schematic picture of the RF-shielded chamber. The gray is ceramic, and the red is a beam with a shift x. The yellows color represents the Cu strips. Each strip is defined by $(r\cos\theta, r\sin\theta)$, with $\theta = 2\pi i/N_s$ and $i = 0, 1, 2, \cdots, N_s - 1$. The conditions meet $x \ll r$ and $r_0 \ll r$

and the line density of image charges becomes

$$\sigma_s' = \frac{\hat{\lambda} e}{2\pi d}. \tag{12}$$

The current on strips is easily given and simplified as

$$I' = I\frac{r}{d}, \tag{13}$$

and the current on a strip is $I_s' = I'/N_s$.

The resistance of the strip is given by

$$R_s = \rho\frac{L_s}{A}, \tag{14}$$

where ρ is the resistivity, L_s is the length of the Cu strips and A is the cross-sectional area. For the skin depth δ_s and width of the rectangular strip w, $A = \delta_s w$.

With the resistance of strips, the voltage across the capacitor is determined by the current flowing through the strip as

$$V = I_s' R_s. \tag{15}$$

The typical parameters of the beam and the ceramic chamber in the RCS are listed in Table 6. For a typical ceramic chamber with $N_s = 66$, the beam intensity peaked at 77 A during extraction, serving as a representative case for voltage estimation. The skin depth $\delta_s = 30\,\mu$m at a typical beam frequency of 5 MHz. Each Cu strip, with a length of 2.1 m, had a resistance of approximately 0.24 Ω. Figure 12 illustrates the voltage on capacitors at different azimuthal angles and a beam with various shifts. It is easy to see that the voltage changes with a horizontal shift and azimuthal angle. For a monopole beam, the voltage on the strip is approximately 0.28 V. In the case of a dipole beam with a 60 mm shift, the maximum voltage on the capacitors was approximately 0.55 V, which was considered negligible compared to the voltage induced by external magnetic fields.

Table 6 Main parameters of beam and chamber in the RCS

Parameter	Values
σ_z at injection/extraction (m)	20/9
β at injection/extraction	0.38/0.93
I_b at injection/extraction (A)	14/77
Length of chamber, L (m)	2.1
Radius of chamber, r (m)	0.1
Strip number, N_s	66
Strip width, w (mm)	5
Strip thickness, t (mm)	0.4
Resistivity of strips (Ω · m)	1.7×10^{-8}

7 Conclusion and outlook

An unexpected transverse instability was detected at low beam powers during the beam commissioning phase in the RCS of CSNS. Subsequent measurements identified this instability as a TCBI. By optimizing the tune and chromaticity, the instability was effectively suppressed, allowing for the current achievement of a 160 kW beam power. However, achieving the 500 kW goal for CSNS-II is challenging. Consequently, studying the sources of impedance

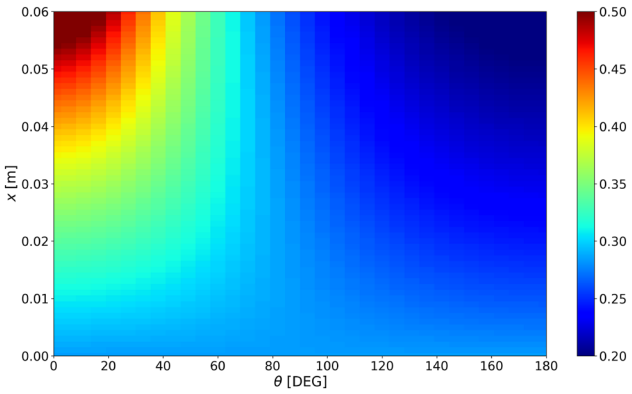

Fig. 12 (Color online) Voltage on capacitors at different azimuthal angles and a beam with a shift x. where a typical ceramic chamber in the RCS with number of Cu strip of 66 and length 2.1 m, and the beam intensity of 77 A with frequency at 5 MHz at extraction is used

remains essential. Beam measurements indicated a possible resonance with a significantly large impedance. Impedance measurements confirmed a resonance associated with the RF shield on the ceramic chamber, which aligned with the frequency observed in the beam measurements. Simulations conducted using the CST Microwave Studio replicated this impedance. As this new impedance cannot be theoretically calculated, we developed an impedance model for the RCS ceramic chambers based on the simulation, providing a foundation for further analysis of the beam effects.

Preliminary numerical simulations provided insights into the physical principles underlying impedance, thereby contributing to the enhancement of the chamber design for impedance reduction. The simulations investigated key parameters such as the chamber length, capacitor capacitance, and effect of the magnet yoke. From a practical and cost-effective perspective, optimizing the capacitor capacitance is a promising approach for reducing the impedance. Although these simulations offer a comprehensive understanding of the impedance characteristics of ceramic chambers and propose effective reduction strategies, thorough validation is required before practical application, with particular attention to the voltage on the capacitors.

This research is currently in its early stages. Although simulation studies have provided valuable insights into the impedance characteristics of the ceramic chamber in the RCS, further research is crucial. This involves exploring additional strategies for impedance reduction and the impact of electromagnetic fields in accelerator tunnels. Moreover, detailed simulation results require interpretation through comprehensive impedance and beam physics theories. Consequently, future work will focus on theoretical analysis and exploration of techniques for reducing impedance.

Acknowledgements The authors would also like to thank Wei-Dong Chen for his discussions and comments on the measurement and simulation. We would like to acknowledge the support of Sheng-Yi Chen, Sheng-Hua Liu and Hai-Bo Li in the measurement.

Author Contributions All authors contributed to the study conception and design. Simulations were conducted by Liang-Sheng Huang, Bin Wu and Yong-Chuan Xiao. The experiment was done by Liang-Sheng Huang, Ren-Hong Liu, Biao Tan and Peng-Cheng Wang. Data collection and analysis were performed by Liang-Sheng Huang. This work was supported by Ming-Yang Huang and Xiao Li. The first draft of the manuscript was written by Liang-Sheng Huang and Li-Rui Zeng, and all authors commented on previous versions of the manuscript. All authors read and approved the final manuscript.

Data Availability The data that support the findings of this study are openly available in Science Data Bank at https://cstr.cn/31253.11.sciencedb.28546 and https://www.doi.org/10.57760/sciencedb.28546.

Declarations

Conflict of interest The authors declare that they have no conflict of interest.

References

1. J. Wei, H.S. Chen, Y.W. Chen et al., China Spallation Neutron Source: Design, R &D, and outlook. Nucl. Instrum. Methods Phys. Res. A **600**(1), 10–13 (2008). https://doi.org/10.1016/j.nima.2008.11.017
2. S. Wang, S.X. Fang, S.N. Fu et al., Introduction to the overall physics design of CSNS accelerators. Chin. Phys. C **33**, 1–3 (2009). https://doi.org/10.1088/1674-1137/33/S2/001
3. L. Dong, J. Zhang, Y. Li et al., Borrowed dislocations for ductility in ceramics. Science **385**(6707), 422–427 (2024). https://doi.org/10.1126/science.adp0559
4. J. Wang, J. Ren, W. Jiang et al., In-beam gamma rays of CSNS Back-n characterized by black resonance filter. Nucl. Sci. Tech. **35**, 164 (2024). https://doi.org/10.1007/s41365-024-01553-8
5. Y. Hong, Y. Song, L. Zhou et al., Beamline design for multipurpose muon beams at CSNS EMuS. Nucl. Sci. Tech. **35**, 38 (2024). https://doi.org/10.1007/s41365-024-01406-4
6. S. Xiao, Y. He, Z. He et al., Driving system design and precision test of the VSANS detector trolleys. Nuclear Techniques (in Chinese) **45**, 090401 (2022). https://doi.org/10.11889/j.0253-3219.2022.hjs.45.090401
7. S. Liu, T. Huang, H. Ouyang et al., Status of CSNS H^- ion source. Chin. Phys. C **39**, 057008 (2015). https://doi.org/10.1088/1674-1137/39/5/057008
8. Y. Xiao, H. Ouyang, K. Xue et al., Development of CSNS RFQ. Nuclear Techniques (in Chinese) **38**, 120201 (2015). https://doi.org/10.11889/j.0253-3219.2015.hjs.38.120201
9. H. Liu, J. Peng, K. Gong et al., The design and construction of CSNS drift tube linac. Nucl. Instrum. Methods Phys. Res. A. **911**, 131–137 (2018). https://doi.org/10.1016/j.nima.2018.10.034
10. J. Peng, Y. Han, Z. Li et al., Beam loss studies in the CSNS Linac. In Proc. of HB'23, Geneva, Switzerland, WEA4C1 297–299 (2023). https://doi.org/10.18429/JACoW-HB2023-WEA4C1
11. S. Wang, Y. An, S. Fang et al., An overview of design for CSNS/RCS and beam transport. Sci. China Phys. Mech. Astron. **54**, 239–244 (2011). https://doi.org/10.1007/s11433-011-4564-x
12. M. Huang, S. Xu, Y. An et al., Study on the anti-correlated painting injection scheme for the Rapid Cycling Synchrotron of the China Spallation Neutron Source. Nucl. Instrum. Methods Phys. Res. A. **1007**, 165408 (2021). https://doi.org/10.1016/j.nima.2021.165408
13. Q. Li, W. Kang, X. Sun et al., Key technology of the development of the CSNS/RCS AC dipole magnet. Power Laser Particle Beams **29**, 085105 (2017).
14. X. Qi, J. Zhang, Z. Hao et al., Magnet power supply system for China Spallation Neutron Source. Power Electron. **48**, 8–10 (2014).
15. S. Xu, The Study on the Space Charge Effects of CSNS/RCS. Beijing: University of Chinese Academy of Sciences 96–99 (2011)
16. H. Dong, H. Song, Q. Li et al., The vacuum system of the China spallation neutron source. Vacuum **154**, 75–81 (2018). https://doi.org/10.1016/j.vacuum.2018.04.046
17. R. Williamson, D. Adams, H. Cavanagh et al., High-Intensity Studies on the ISIS RCS and Their Impact on the Design of ISIS-II. In Proc. of HB'23. Geneva, Switzerland, TUC4I2 331–337 (2023). https://doi.org/10.18429/JACoW-HB2023-TUC4I2
18. Accelerator Technical Design Report for High-Intensity Proton Accelerator Facility Project. JAERI Report No. JAERI-Tech 2003-044 and KEK Report No. 2002-13. (2003)
19. R. Williamson, D. Adams, B. Jones et al., Simulation of the head-tail instability on the ISIS synchrotron. In Proc. of HB'14. East-Lansing, MI, USA 113 (2014)
20. D.W. Posthuma de Boer, B.A. Orton, C. M. Warsop et al., Development of an impedance model for the ISIS synchrotron

and predictions for the Head-Tail instability. In Proc. of HB'23. Geneva, Switzerland, TUC4I2 170–177 (2023). https://doi.org/10.18429/JACoW-HB2023-THA1I2
21. Y. Shobuda, H. Harada, H. Hotchi, et al., Measurement result of the impedance of the RF-cavity at the RCS in J-PARC. In Proc. of IPAC'15. Richmond, VA, USA, MOPWA058 255 (2015). https://doi.org/10.18429/JACoW-IPAC2015-MOPWA058
22. L. Huang, M. Huang, S. Xu et al., Intense beam issues in CSNS accelerator beam commissioning. In Proc. of HB'23. Geneva, Switzerland, MOA1I3 16–22 (2023). https://doi.org/10.18429/JACoW-HB2023-MOA1I3
23. S. Xu, H. Liu, J. Peng et al., Beam commissioning and beam loss control for CSNS accelerators. JINST **15**, P07023 (2020). https://doi.org/10.1088/1748-0221/15/07/P07023
24. L. Huang, Y. An, C. Deng et al., Upgrade of the sextupole field for beam instability mitigation in rapid cycling synchrotron of China Spallation Neutron Source. Radiat. Detect. Technol. Methods **7**, 550–560 (2023). https://doi.org/10.1007/s41605-023-00428-7
25. A.W. Chao, *Physics of Collective Beam Instabilities in High Energy Accelerators* (Wiley, New York, 1993), p.15
26. H. Xu, C. Lin, N. Wang et al., Transverse mode-coupling instability with longitudinal impedance. Nucl. Sci. Tech. **35**, 103 (2024). https://doi.org/10.1007/s41365-024-01472-8
27. J. Su, Y. Liu, S. Tian et al., Longitudinal impedance measurements and simulations of a three-metal-strip kicker. Nucl. Sci. Tech. **34**(4), 57 (2023). https://doi.org/10.1007/s41365-023-01212-4
28. Y. Liu, L. Huang, S. Wang et al., Impedance and beam instability in RCS/CSNS. High Power Laser and Particle Beams **25**, 465–470 (2013). https://doi.org/10.3788/hplpb20132502.0465
29. L. Huang, Y. Liu, S. Wang, Resistive wall instability in rapid cycling synchrotron of China Spallation Neutron Source. Nucl. Instrum. Meth. Phys. Res. Sect. A **728**, 1–5 (2013). https://doi.org/10.1016/j.nima.2013.06.017
30. L. Huang, S. Wang, Y. Liu et al., Impedance measurements of the extraction kicker system for the rapid cycling synchrotron of China Spallation Neutron Source. Chin. Phys. C **40**(4), 047002 (2016). https://doi.org/10.1088/1674-1137/40/4/047002
31. N. Wang, Q. Qin, Resistive-wall impedance of two-layer tube. Phys. Rev. Accel. Beams **10**, 111003 (2007). https://doi.org/10.1103/PhysRevSTAB.10.111003
32. Physics design and technology development of CSNS accelerator. Institute of High Energy Physics, IHEP Report, Beijing, China (2010)
33. L. Huang, S. Wang, S. Xu et al., Source of instability in the rapid cycling synchrotron of the China spallation neutron source. Eur. Phys. J. Plus **140**(1), 71 (2025). https://doi.org/10.1140/epjp/s13360-025-05997-8
34. B. Zotter, Longitudinal instabilities of charged particle beams inside cylindrical walls of finite thickness. Particle Accelerators **1**, 311–326 (1970)
35. A.W. Chao, M. Tigner, *Handbook of accelerators physics* (Singapore, World scientific, 1999), p.205
36. Y. H. Chin, S. Lee, K. Takata et al., Impedance generated by a ceramic chamber with RF shields and TiN coating. In proc. of HB'06, Tsukuba, Japan, TUBX01 (2006)
37. N. Wang, Coupling impedance and collective e ects in the RCS ring of the China spallation neutron source. Ph. D thesis, University of Chinese Academy of Sciences (2009)
38. F. Roncarolo, F. Caspers, T. Kroyer et al., Comparison between laboratory measurements, simulations and analytical predictions of the transverse wall impedance at low frequencies. Phys. Rev. Accel. Beams **12**, 084401 (2009). https://doi.org/10.1103/PhysRevSTAB.12.084401
39. V. Danilov, S. Henderson, A. Burov et al., An improved impedance model of metallic coatings. In proc. of the EPAC'02 1464–1466 (2002)
40. CST STUDIO SUITE website. https://www.3ds.com/products/simulia/cst-studio-suite
41. K.Y. Ng, *Physics of Intensity Dependent Beam Instabilities* (World Scientific, Singapore, 2006)
42. F. Caspers. Bench methods for beam-coupling impedance measurement. CERN report, CERN PS/88–59 (1988)
43. A. Mostacci, F. Caspers, U. Iriso et al., Bench measurements of low frequency transverse impedance. In proc. of PAC'03, pp. 1801–1803 (2003)
44. H. Hotchi, H. Harada, N. Hayashi et al., Achievement of a low-loss 1-MW beam operation in the 3-GeV rapid cycling synchrotron of the Japan Proton Accelerator Research Complex. Phys. Rev. Accel. Beams **20**, 060402 (2017). https://doi.org/10.1103/PhysRevAccelBeams.20.060402